

**Reflux-synthesized bulk and supported W-Nb-O mixed oxide bronzes
for the valorization of short-chain oxygenates aqueous mixtures**

D. Delgado, A. Fernández-Arroyo, N. La Salvia, M.E. Domine*,

and Jose M. López Nieto*

Instituto de Tecnología Química, Universitat Politècnica de València-Consejo Superior
de Investigaciones Científicas, Avenida de los Naranjos s/n, 46022, Valencia, Spain.

E-mail: jmlopez@itq.upv.es;

Abstract

This work reports the preparation of bulk and KIT-6-supported W-Nb-O mixed oxide bronzes by a reflux method. The influence of the incorporation of Nb and a mesoporous silica on the physicochemical features of the catalysts is studied. The addition of Nb favors the formation of single-phase oxide bronze structure, with improved Lewis acidity; while the incorporation of KIT-6 gives rise to well-dispersed mixed metal oxide particles on the support. Supported W-Nb-O catalysts present enhanced surface areas and mesopore volumes. The materials have been tested in the valorization of an aqueous model mixture (acetol/propanal/ethanol/acetic acid/water weight ratio of 5/25/10/30/30), through C-C bond formation reactions. The increase in the Lewis nature of surface acid sites stands as the key point to maximize the total organic yield during the reaction (C₅-C₁₀ products). The best catalysts maintain their catalytic behavior after five consecutive uses.

Keywords: KIT-6; W-Nb-O oxides; aqueous oxygenates; biomass feedstocks; C-C bond formation

1. Introduction

Tungsten oxide bronzes and related compounds are probably, among all metal oxide families, one of the most versatile systems in terms of composition, crystal structure and applications [1, 2]. These materials are able to accommodate a vast variety of elements (even present in mixed oxidation state) within their crystal framework, which usually undergoes through the generation of several structural defects, such as crystallographic shear planes (i.e. Wadsley defects) [3] or rotational faults (leading in some cases to the formation of tunnel structures) [4]. The possibility to vary both composition and structural characteristics paves the way to functional properties modulation. Particularly, tungsten oxide bronze-based materials have found applications in a wide range of fields, like superconductivity [5], magnetic materials [6], electrochromics [7] or gas sensing [8]. Despite this, the catalytic application of these oxides are scarce, mainly because they usually show extremely low surface areas, derived from synthesis methods based on solid state reactions. According to this, the development of new synthetic strategies becomes pivotal to extend the use of this large family of materials to catalysis science.

Among the examples of tungsten oxide bronzes with interesting catalytic properties we can point out hydrothermally synthesized tetragonal tungsten bronzes for the partial oxidation of propylene [9] and the catalytic abatement of trichloroethylene [10], or hexagonal tungsten bronze materials (prepared either by hydrothermal or reflux methods) for the aerobic transformation of glycerol into acrolein and acrylic acid [11-13]. Also they have been applied in alkylation reactions [14] or as electrocatalysts [15].

Recently, we showed that a pseudocrystalline niobium oxide, prepared by hydrothermal synthesis, was highly efficient in the valorization of an aqueous model mixture of short-

chain oxygenates [16]. The reaction mixture used in this study resembled the aqueous waste stream obtained after the treatment of a pyrolytic bio-oil by water addition and phase separation, which we were able to transform into longer carbon chain molecules, useful for blending with conventional fuels [17]. According to the complex chemical nature of biomass feedstocks, it becomes difficult to avoid the generation of residues, when dealing with their transformation into fuels or chemicals [18]. In fact, the valorization of these streams stands as one of the central points in the development of bio-refineries.

The most extended approach to pyrolysis bio-oil upgrading is hydrotreating [19]. Supported on well-established hydrocracking and HDO technologies, it consists in pyrolytic oil treatment at high temperature and H_2 pressures, in the presence of CoMo, and/or NiMo-based catalysts [20]. These methodologies give rise to a bio-oil with good fuel properties. However, low fuel-yields (most of low molecular weight molecules are transformed into gases) and high H_2 consumption are their main disadvantages.

Recently, a new approximation to the problem has been developed, which consists in the pyrolytic oil treatment by water addition [21]. The addition of water leads to phase-separation into two fractions. The organic fraction can be further treated by conventional methods to lead a bio-fuel suitable for automotive uses. On the other hand, the aqueous phase, containing most of short-chain oxygenates, still remains as a residue. Then, the development of new pathways to the valorization of this streams would help to increase the atom economy and decrease the costs of the process.

Herein we report the reflux synthesis of a series of bulk and KIT-6-supported W-Nb-O mixed oxide catalysts for the valorization of short-chain oxygenated compounds present in aqueous mixtures by C-C bond formation reactions. The aqueous model mixture used

in the catalytic tests resembles that obtained from pyrolytic bio-oils upgrading processes, by means of water addition and phase separation. The effect of the incorporation of both Nb and the siliceous support on the physicochemical characteristics of the materials is discussed, as well as their catalytic implications.

2. Experimental

2.1. Catalyst preparation

KIT-6 mesoporous silica was prepared according to the method reported by Kleitz et al. [22], using Pluronic P123, n-butanol and TEOS as precursors. Bulk and supported W-Nb oxide bronzes were prepared from acidified aqueous solutions containing the following metal salts: ammonium metatungstate hydrate (≥ 85 wt% WO_3 , Sigma-Aldrich) and niobium oxalate monooxalate adduct (ABCR). Nb/(W+Nb) at. ratios used in the synthesis were 0.10, 0.20 and 0.60 (A, B and C series of catalysts, respectively). The solutions were kept under reflux at 150 °C for 48 h. In the case of supported W-Nb-O oxides, different amounts of mesoporous KIT-6 silica were added after the reflux treatment. A rotary evaporator was used to eliminate the solvent. Resulting solids (both bulk and supported catalysts) were then dried at 100 °C overnight and subsequently heat-treated at 400 °C for 2h in N_2 flow. Catalysts are named as A-X, B-X or C-X, being X the amount of KIT-6 support added in wt%; and A, B and C, represent the specific Nb/(W+Nb) ratio in the materials (0.10, 0.20 and 0.60, respectively).

For comparison, an undoped hexagonal tungsten bronze ($h\text{-WO}_3$) was also synthesized, according to a standard hydrothermal procedure [23].

2.2. Characterization

Powder X-Ray diffraction (XRD) analyses were carried out in a PANalytical X'Pert PRO diffractometer, using CuK α radiation. The instrument was equipped with a X'Celerator X-ray detector in a Bragg-Brentano geometry.

N₂-adsorption isotherms were collected in a Micromeritics ASAP 2000 device. Samples were outgassed at 300 °C in vacuum prior to N₂ adsorption. Surface areas and mesopore volumes were calculated by Brunauer-Emmett-Teller (BET) and Barrett-Joyner-Halenda (BJH) methods, respectively.

Analysis by Scanning electron microscopy (SEM) were performed in field emission ZEISS Ultra microscope. Images were collected at an accelerating voltage of 2 kV.

High resolution electron microscopy (HRTEM) images were obtained in a JEOL JEM 2100F electron microscope at 200 kV of accelerating voltage.

Experiments of FTIR of adsorbed pyridine were performed in a Nicolet 710 spectrometer. The catalysts were introduced into the IR cell in the form of self-supported wafers of 10 mg cm⁻², which were degassed in vacuum at 300 °C for 2h prior to the adsorption of pyridine. Then, pyridine was admitted (6.5 x 10⁻² Pa) and, when equilibrium is achieved, samples were outgassed at 150 °C, and cooled to room temperature. Afterwards pyridine sorption FTIR spectra were measured. Samples were then subsequently heated at 250 °C and cooled down to room temperature again. Then, a second spectrum was collected. A spectrum measured before pyridine adsorption was subtracted from each of the spectra measured (i.e. spectra after desorption at 150 and 250 °C). All the spectra were normalized to sample weight before data treatment. The concentration of acid sites after degassing at 150 and 250 °C were calculated from band areas according to the method reported by Emeis [24].

2.3. Catalytic tests

The catalytic tests were carried out under stirring in a 12 ml PEEK-lined (polyether-ethyl-ketone) autoclave reactors, equipped with pressure control and a valve for either liquid or gas sample extraction. Reactors were placed over a steel jacket equipped with a temperature close loop control system.

The feed consisted of an aqueous mixture containing short-chain oxygenated compounds (acetol/propanal/ethanol/acetic acid/water wt% ratio 5/25/10/30/30). The composition simulates that of a waste stream derived from the aqueous phase separation of a pyrolytic bio-oil. The experiments were conducted using 3.0 g of aqueous model mixture and 0.15 g of catalyst, which were introduced in the autoclave-type reactor. The autoclave was sealed and pressurized at 13 bar of N₂. The reactions were performed at 200 °C under continuous stirring during 7 h of reaction.

Liquid aliquots of 50-100 µl were taken, filtered off and diluted in 0.5 g of methanol containing 2 wt% chlorobenzene used as standard for the GC analysis. The solutions were analyzed in a Bruker 430 GC equipped with a FID detector and a capillary column (TRB-624, 60 m length).

Identification of the products was carried out by GC-MS (Agilent 6890 N GC System coupled with an Agilent 5973 N mass detector and equipped with a HP-5 MS, 30 m length capillary column).

Reactants and products were quantified from GC-FID response factors calculated by calibration with the use of an internal standard, while long-chain products were classified in intervals (C₅-C₈ and C₉-C₁₀) and group contribution technique was used to predict their corresponding response factors. Catalytic results in this work are discussed in terms of reactant conversion and main reaction products yield. Thus, yields to 2-methyl-2-pentenal

(2M2P), other C₅-C₈ compounds, and C₉-C₁₀ products, as well as total organic products yield (sum of 2M2P, C₅-C₈ and C₉-C₁₀ products) are reported. More information is detailed in SI.

Acetic acid (99.8%), propanal (97%), acetol (90%) and chlorobenze (99%) were purchased from Sigma-Aldrich and used as received. Ethanol (99.9%), methanol (99.9%) supplied by Scharlau and water (Milli-Q quality, Millipore) were used as solvents.

3. Results and discussion

3.1. Characterization of bulk and supported W-Nb-O oxides

Figure 1 displays powder XRD patterns of bulk and KIT-6-supported W-Nb-O catalysts. For comparative purposes, the diffractogram corresponding to a *h*-WO₃ oxide, synthesized by a standard hydrothermal procedure [23], is also represented.

The structural features of W-Nb-O oxides are highly dependent on Nb content, as deduced from the changes observed in the XRD profiles for A, B and C series of catalysts (**Fig. 1**, A-C). At low Nb contents (i.e. Nb/(W+Nb) at. ratio of 0.10 and 0.20, A-series and B-series, respectively), all the catalysts present the characteristic Bragg peaks of a hexagonal tungsten bronze-type structure (JCPDS: 33-1387) (**Fig. 1A** and **Fig. 1B**). This structure is characterized by the presence of corner-sharing MO₆ octahedra displaying 3- and 6-member rings along [001] direction (**Fig. 1**) [25]. We must mention that the attempt to synthesize a single-phase undoped hexagonal tungsten bronze by this reflux method was unsuccessful. The XRD diagram of the as-synthesized material shows the corresponding reflections of tungstite (JCPDS: 43-0679), *h*-WO₃ (JCPDS: 33-1387) and W₁₈O₄₉ (JCPDS: 05-0392) (**Fig. S1**). It has been proposed that the formation of bronze-type

structures by soft chemistry methods can be favored when specific polyoxometalate-like species are formed in solution [26-28]. These structures are the donors of the building blocks and linkers that give rise to the metal oxide structure. The fact that the single-phase metal oxide bronze is only obtained when Nb^{5+} species in solution suggests that they could be acting as a “linkers” between tungstate species, assisting the formation of the hexagonal tungsten bronze structure. When the amount of Nb is further increased (up to Nb/(W+Nb) at. ratio of 0.60, C-series), the resulting XRD profiles are completely different (**Fig. 1C**). They just show two clear diffraction signals, which correspond to 001 and 002 planes, at 2θ values of ca. 23 and 26 °, displaying also some broad maxima centered at ca. 27, 35, 48 and 55 °. Then, when high Nb amounts are incorporated, it is difficult to ascribe the distribution of tungsten and niobium atoms to a specific crystal structure. Despite this, the connection between octahedra remains, as deduced from the well-defined 001 and 002 lines, which indicate long-range order, at least along *c*-axis direction ($c \approx 3.8 \text{ \AA}$).

In addition, the incorporation of KIT-6 as support does not modify the structural characteristics of the oxides, according to the similar distribution of diffraction lines found for bulk and supported materials in each series (**Fig. 1, A-C**).

According to these results, the following structural implications can be underlined: i) The presence of low amounts of Nb^{5+} favors the formation of a single phase hexagonal tungsten bronze oxide, ii) higher Nb/(W+Nb) ratios in the synthesis provoke a loss of long range order in the *ab* plane of the structure, leading to pseudocrystalline oxides and; ii) W-Nb-O crystal structure does not vary after the incorporation of the mesoporous support.

The nature of metal-oxygen bonds in the materials was investigated by means of Raman spectroscopy. **Figure 2** displays Raman spectra of selected bulk (**Fig. 2A**) and supported (**Fig. 2B**) catalysts. For comparative purposes, the corresponding Raman spectrum of a *h*-WO₃ oxide is also shown. All the materials show bands at 691 and 780 cm⁻¹, which are assigned to O-W-O stretching modes in the bronzes [29]. When Nb is incorporated, a new signal at approximately 749 cm⁻¹ appears in the spectra (**Fig. 2**, a-d). Since Raman bands associated to the presence of Nb₂O₅ (at ca. 700 cm⁻¹) [30] are not observed in any case, we can tentatively assign this feature at 749 cm⁻¹ to W-O-Nb stretching modes. In fact, the relative intensity of this band increases proportionally with Nb concentration in the catalysts. The broad band centered at 952 cm⁻¹ can be ascribed to M=O (M: W, Nb) stretching vibrations [31, 32], while the features appearing at lower frequencies (200-400 cm⁻¹) are assigned to O-M-O deformation modes [29]. Interestingly, all Nb-containing spectra show broader signals, in agreement with a lower order degree in the oxide framework. Thus, pseudocrystalline oxides show the broadest Raman profiles. Also, both bulk and supported materials display essentially the same profile, regardless of whether KIT-6 is added as support or not. All these features found in Raman spectra are in line with the specific characteristics observed previously by XRD.

Although the addition of an inert mesoporous support does not have substantial structural consequences, it can have a major effect on the textural properties of the catalysts. **Figure S2** shows N₂-adsorption isotherms of selected bulk and supported W-Nb bronzes. For comparison, the isotherm of KIT-6 silica is also included (**Fig. S2**, A). The corresponding BET surface areas and mesopore volumes are included in **Table 1**. The analysis of the isotherms by BET method indicates an increase in the surface area and mesopore volume for supported materials (**Table 1**). Moreover, focusing on specific adsorption-desorption branches of supported oxides, they display additional features, i.e. changes in the slope

of the isotherm profiles (**Fig. S2**, B and C), with respect to unsupported catalysts (**Fig. S2**, D and E). This suggest the presence of pores with well-defined size.

In a previous work we showed that, after the preparation of supported catalysts, KIT-6 silica losses its long-range ordered structure [11]. In order to get further insights on this issue we have represented BJH plots of bulk and supported W-Nb-O catalysts with a Nb/(W+Nb) ratio 0.10 (A Series) (**Fig. S3**, a to c). It can be seen that all the samples present a maximum around 8-10 nm, that can be ascribed to the channels of the mesoporous KIT-6, according to BJH profile of as-synthesized support (**Fig. S3, d**). Then, although the ordered structure is lost, the support still maintains some remaining mesoporosity, what would explain both the increase in surface areas and mesopore volumes observed in supported W-Nb-O oxides (**Table 1**).

Figure 3 shows SEM micrographs of crystalline and pseudocrystalline bulk and supported W-Nb-O catalysts. Bulk materials (**Fig. 3**, A and B) show platelet-shaped particles, whose size decreases at higher Nb concentration (**Fig. 3B**). This would explain the higher surface area observed for bulk materials with higher Nb-contents (**Table 1**). **Figure 3C** displays a SEM micrograph of KIT-6 support, which display round-shaped particles with diameters in the range 2-5 μm . When W-Nb-O bronzes are deposited on the siliceous support, images show small mixed-oxide particles well-dispersed on ball-like mesoporous silica (**Fig. 3D**).

HRTEM images of as-synthesized support, and crystalline and pseudocrystalline supported W-Nb-O oxides are shown in **Figure 4**. As-prepared mesoporous support displays a well-ordered porous structure, ascribed to KIT-6 polymorph, showing pores with a diameter of ca. 10 nm (**Fig. 4A**) [22]. This well-ordered mesopore distribution is no longer observed after the preparation of supported oxides. In the case of supported

catalysts, oxides with a hexagonal tungsten bronze structure show the presence of crystals with the characteristic distribution of hexagonal channels in the *ab* plane of the structure (**Fig. 4B**). On the other hand, pseudocrystalline W-Nb-O supported oxides only present clear interplanar spacings of ca. 3.8 Å, which can be assigned to 001 planes of the disordered phase (**Fig. 4C**). These observations underline the loss of periodicity observed at high Nb-contents, which lead to ordered materials just along [001] direction of the structure.

This pseudocrystalline oxide have been assigned in some cases to a $\text{Cs}_{0.5}\text{W}_{2.5}\text{Nb}_{2.5}\text{O}_{14}$ -type phase [33], isostructural with the well-known M1-type MoVTaNbO partial oxidation catalyst [34, 35]. These materials show a similar XRD pattern found in our catalysts with high Nb-contents (C-series). In our case, we were not able to find any crystal presenting the characteristic atom distribution of the M1-phase, as it was shown for hydrothermally synthesized catalysts. It is very likely that hydrothermal method (which in fact is the most extended strategy to obtain these materials) could favor the formation of well-ordered structures in the *ab*-plane, at least in a higher extent than reflux-methodologies. Nevertheless, as far as electron microscopy techniques are concerned, analyzed areas are very small in comparison with the whole extension of the material, what would make it difficult to find these well-ordered particles in our catalysts if their concentration is low.

The acid features of selected bulk and supported W-Nb-O bronzes were studied by means of FTIR of adsorbed pyridine. **Figure 5** displays pyridine sorption FTIR spectra after the evacuation at 150 and 250 °C (**Fig. 5**, a-d and a'-d', respectively), whereas the quantitative analyses of acid sites concentration are shown in **Table 2**.

All the catalysts display the characteristic FTIR signals due to: i) ring bending modes of pyridinium ion (band at 1538 cm^{-1}), formed by the interaction of pyridine with Brönsted

sites (i.e. Py-H⁺ in **Figure 6**); and ii) ring modes of pyridine coordinatively bonded to Lewis centers through its nitrogen electron lone-pair (band at 1450 cm⁻¹) (i.e. Py-L in **Figure 6**) [24, 36]. By measuring peak areas corresponding to each type of site, we can estimate the amount of both surface Lewis and Brönsted acid sites [24]. In turn, by comparing peak intensities at two desorption temperatures (i.e. 150 and 250 °C), it is also possible to estimate the acid strength of those sites [36].

The catalysts show different Py-H⁺ and Py-L peak intensities depending on Nb concentration and the desorption temperature applied in the experiments (**Fig. 5**). Specifically, all Nb-containing catalysts show a higher concentration of acid sites than *h*-WO₃ sample, as it can be deduced from the higher peak areas in the spectra measured after pyridine desorption at 150 °C (**Fig. 5**, spectra a to d) (**Table 2**). In addition, the incorporation of Nb within the crystal framework of tungsten oxide leads to changes in the relative intensity of Py-H⁺ and Py-L peaks (**Fig. 5**). Particularly, the incorporation of Nb gives rise to an increase in the relative intensity of Py-L signal, indicating an increase in the concentration of Lewis acid sites (**Fig. 5**) (**Table 2**).

When comparing peak intensities at 150 and 250 °C, it can be observed that the intensity of peaks ascribed to pyridine bonded to both Lewis and Brönsted sites decreases for the highest desorption temperature (**Fig. 5**, spectra a'-d'). Interestingly, the peak assigned to Brönsted sites disappears after pyridine desorption at 250 °C for the samples with the highest Nb content, i.e. for pseudocrystalline materials (**Fig. 5**, spectra c' and d'). This fact indicates a decrease in the acid strength of Brönsted sites, especially at high Nb contents. On the contrary, Py-L signal intensity decreases in the same extent for all the catalysts, what suggest similar acid strength of Lewis sites, regardless of the amount of Nb incorporated in the structure.

3.2. Catalytic properties in the transformation of short-chain oxygenates

All the catalysts have been tested in the valorization of an aqueous mixture containing acetol, propanal, ethanol and acetic acid (acetol/propanal/ethanol/acetic acid/water wt% ratio 5/25/10/30/30). The approach in this sense is to increase the carbon chain length of organic compounds in the mixture by performing acid-catalyzed C-C bond formation reactions, particularly aldol condensation. A scheme of the valorization strategy is depicted in **Figure S4** in Supporting Information. For instance, two propanal molecules can react via self-aldol condensation, yielding 2-methyl-2-pentenal (2M2P) (C₆ product). Subsequently, 2M2P can further react with another propanal molecule, leading to 2,4-dimethyl-2,4-heptadienal as aldol condensation product (C₉ product). In addition, acetone produced via acetic acid ketonization and acetol could participate in condensation reactions. The combination of aldol condensation of different molecules together with consecutive dehydration and intramolecular cyclization pathways could explain most of the reaction products detected by GC-MS; which have been grouped as C₅-C₈ and C₉-C₁₀ products (see additional information and **Figs. S5** and **S6**, in Supporting Information). Nevertheless, due to the complexity of the reaction mixture and the presence of multiple compounds, it is very difficult to assess the specific reaction pathways for the generation of these compounds with some confidence. More interestingly, these longer carbon chain products could be interesting for fuel blending.

The reactions were carried out in PEEK-lined autoclave reactors at relatively mild conditions ($P_{N_2} = 13$ bar, 200 °C, $m_{cat} = 150$ mg) during 7 h. Catalytic results are summarized in **Table 3**, where total organic yield is referred to products in C₅-C₁₀ range.

Figure 6 displays the degree of conversion of each oxygenated compound in the aqueous mixture for bulk and supported W-Nb-O bronzes. The conversion of reactants lays in the

range 80-93%, 44-53% and 0-10%, for propanal, ethanol and acetic acid, respectively; while all the catalysts show a 100% acetol conversion (**Table 3**). We must note that: i) only Nb-containing catalysts are able to transform acetic acid (although the conversion is low) and, ii) that ethanol conversion slightly decreases at higher Nb concentration in the materials. Also, if we attend to the effect of the support, a slight decrease in the conversion of propanal is observed in most of supported catalysts with respect to bulk W-Nb-O oxides in each series.

Although the conversion of the different mixture components does not vary significantly among the different series, i.e. regardless of the amount of Nb incorporated, we must underline that Nb-content has a mayor influence on the product distribution. **Figure 7** shows the yield to the different reaction products for bulk and supported W-Nb-O catalysts (2-methyl-2-pentenal, C₅-C₈ and C₉-C₁₀ products). Additionally, the main by-product obtained all along the series was ethyl acetate, which can be formed via esterification of acetic acid with ethanol (yields in the range 20-23wt%) (**Table 3**). The main reaction product found in all cases is 2M2P, formed through self-aldol condensation of propanal (2M2P yields in the range 28-35 wt%) (**Fig. 7A**) (**Table 3**). In this sense, the formation of 2M2P as first condensation product increases concomitantly with the incorporation of Nb in the materials. However, if we include all C₅-C₈ detected products (which can be assumed to be intermediates of the formation of C₉-C₁₀ compounds), we observe: i) an increase in the yield to C₅-C₈ for all Nb-containing catalysts with respect to undoped *h*-WO₃ but, ii) a decrease in the yield to these products when Nb concentration increases in W-Nb-O oxides (**Fig. 7B**). This effect can be explained if we take into consideration C₉-C₁₀ yields observed along the series, which increases proportionally with Nb in the oxides. It is worth mentioning that the decrease in C₅-C₈ yield and the subsequent increase in the C₉-C₁₀ yield suggests that long chain products are formed by

aldol-condensation of C₅-C₈ intermediates with smaller molecules, like propanal or acetol. Accordingly, if we group all C₅-C₈ and C₉-C₁₀ products, the total organic yield increases progressively at increasing amounts of Nb in the tungsten bronze (**Fig. 8**). Then, it becomes clear that the incorporation of Nb within tungsten oxide framework favors first and second condensation paths, maximizing the total organic yield.

The effect of Brönsted/Lewis acid sites ratio on the transformation of small oxygenates has been widely addressed in the literature. For example, it has been reported that Brönsted acid/base pairs direct the reactivity through esterification reactions, while Lewis acid/base sites would favor aldol condensation pathways [37, 38]. According to the specific acid characteristics of our catalysts, measured by FTIR of adsorbed pyridine, we can ascribe this improved catalytic performance (i.e. an increase in the yield to condensation products) to an increase in the Lewis acidity, and more specifically in the Lewis to Brönsted acid sites ratio (LAS/BAS) (see Table 2) promoted by the incorporation of Nb, especially for materials from C-series (i.e. Nb/(W+Nb) = 0.6). The presence of higher amounts of Brönsted acid sites (LAS/BAS close to 1) favors the occurrence of competitive reactions catalyzed by Brönsted acidity, such as esterification of acetic acid, among others. As a result, lower amounts of C₅-C₈ and C₉-C₁₀ products are formed, this lowering the total organic products yields. This general catalytic behaviour is observed in Figure 8, where the total organic yields of the catalysts series here studied increased in the order: A-series < B-series < C-series. Moreover, it is very likely that the pseudocrystalline nature of these materials with high Nb concentrations, showing highly distorted *ab* crystal planes, could also help to increase the Lewis acid nature of the oxides. In this respect, the amorphization in the *a-b* plane can derive in a higher concentration of coordinatively unsaturated sites, i.e. Lewis acid centers in which condensation paths are favored. In addition, the differences between the catalytic

materials due to the presence of mesoporosity and well-defined mesoporous structure by the incorporation of KIT-6-type material, could significantly affect the total organic yield observed, and mainly the selectivity to the C5-C8 and C9-C10 products. Therefore, although the presence of Lewis acid sites and the LAS/BAS ratio are the main reasons for the higher production of heavier organic compounds, the positive influence of KIT-6 mesoporous structure could result in a synergetic effect.

Finally, we have undertaken stability tests on W-Nb-O catalyst with the highest Nb/(W+Nb) ratios (catalysts from C-series). When dealing with such complex aqueous mixtures, derived from pyrolytic bio-oil upgrading, we must bear in mind that the catalyst chosen must be able to work under low pH conditions (due to high concentration of acetic acid) and at high water contents. To evaluate the resistance of bulk and supported W-Nb-O catalysts (C-series) we have performed 5 consecutive uses under the same reaction conditions (**Fig. S7**). Only a slight decrease in the total organic yield is observed for both catalysts after the fifth use. Interestingly, XRD patterns of the used catalysts show no decomposition of the catalysts (**Fig. S8**, supporting information). Only a small amount of carbon deposits (2-5 wt%) is found on the catalysts after the third use, which could explain the slight catalyst decay. Nevertheless, no leaching of the active components was detected after the reactivity tests, which demonstrates the high resistance of these materials under relatively high demanding conditions.

4. Conclusions

A series of bulk and KIT-6 supported W-Nb-O bronzes have been synthesized by a reflux method, in which the amount of both Nb and mesoporous support has been varied systematically. It has been observed that the incorporation of Nb in the synthesis favors

the formation of single-phase bronze structures. At low Nb-concentration (i.e. Nb/(W+Nb) at. ratios of 0.10 and 0.20) the catalysts present a hexagonal tungsten bronze structure, in which Nb is incorporated within the framework. The incorporation of higher amounts of Nb leads to a loss of periodicity in the *ab* plane of the crystal structure, giving rise to pseudocrystalline materials with long-range order just along *c* direction. The inclusion of Nb within tungsten oxide lattice also gives rise to changes in the acid characteristics of the catalysts: i) the proportion of Lewis surface acid sites increases and; ii) the acid strength of Brönsted acid sites decreases.

The incorporation of KIT-6 support does not have significant effects on the catalysts crystal structure, showing a major influence on the textural properties of the materials. This way, although its ordered mesoporous structure is lost, the catalysts still present remaining mesoporosity. Subsequently, surface areas and mesopore volumes increase, concomitantly with the amount of silica loaded. Electron microscopy analyses show a well dispersion of W-Nb mixed oxides on KIT-6 silica.

Bulk and Supported W-Nb-O catalysts have been tested in the valorization of aqueous mixtures of short chain oxygenates (acetol/propanal/ethanol/acetic acid/water wt% ratio 5/25/10/30/30). The model aqueous mixture has been designed taking into consideration the composition of waste aqueous streams derived from bio-oils upgrading by water addition and phase separation (i.e. it presents a relatively high water and acetic acid content). The majority compounds detected after reaction ($P_{N_2} = 13$ bar, 200 °C, 7 h) were first (C₅-C₈) and second (C₉-C₁₀) aldol condensation products. The total organic yield increases with the concomitant increase of the concentration of Nb in the catalysts, suggesting an improved catalytic performance at higher Lewis/Brönsted acid sites ratio. The best catalysts, with (Nb/(W+Nb) at. ratio of 0.60, maintain their catalytic activity after five consecutive uses

Acknowledgements

Financial support by the Spanish Government (CTQ-2015-68951-C3-1, CTQ-2015-67592, and SEV-2016-0683) is gratefully acknowledged. DD and AF-A thank the Severo Ochoa Excellence Program (SVP-2014-068669) and the “La Caixa-Severo Ochoa” Foundation, respectively, for their fellowships. NS and DD thank “Conselho Nacional de Desenvolvimento Científico y Tecnológico (CNPq)” in Brasil. Authors are also grateful to the Electron Microscopy Service (Universitat Politècnica de València) for facilities.

5. References

- [1] D. J. M. Bevan, in: D. J. M. Bevan, P. Hagenmuller eds., Non-Stoichiometric Compounds, Pergamon, **1973**, 453-540.
- [2] P. Hagenmuller, in: D.J.M. Bevan, P. Hagenmuller eds., Non-Stoichiometric Compounds, Pergamon, **1973**, 541-605.
- [3] J. S. Anderson, R. J. D. Tilley, in: M. W. Roberts, J. M. Thomas eds., Surface and Defect Properties of Solids: Volume 3, The Royal Society of Chemistry, **1974**, 1-56.
- [4] L. A. Bursill, B. G. Hyde, Nature-Phys. Sci., **1972**, 240, 122-124.
- [5] C. J. Raub, A. R. Sweedler, M. A. Jensen, S. Broadston, B. T. Matthias, Phys. Rev. Lett., **1964**, 13, 746-747.
- [6] M. Leblanc, G. Ferey, Y. Calage, R. De Pape, J. Solid State Chem., **1984**, 53, 360-368.
- [7] E. Masetti, D. Dini, F. Decker, Sol. Energy Mater Sol. Cells, **1995**, 39, 301-307.
- [8] I. M. Szilágyi, S. Saukko, J. Mizsei, A.L. Tóth, J. Madarász, G. Pokol, Solid State Sci., **2010**, 12, 1857-1860.
- [9] P. Botella, B. Solsona, E. García-González, J. M. González-Calbet, J. M. López Nieto, Chem. Commun., **2007**, 5040-5042.
- [10] N. Blanch-Raga, M. D. Soriano, A. E. Palomares, P. Concepción, J. Martínez-Triguero, J. M. López Nieto, Appl. Catal. B: Env., **2013**, 130-131, 36-43.

- [11] N. La Salvia, D. Delgado, L. Ruiz-Rodríguez, L. Nadji, A. Massó, J. M. López Nieto, *Catal. Today*, **2017**, 296, 2-9.
- [12] D. Delgado, A. Chieragato, M. D. Soriano, E. Rodríguez-Aguado, L. Ruiz-Rodríguez, E. Rodríguez-Castellón, J. M. López Nieto, *Eur. J. Inorg. Chem.*, **2018**, 2018 1204-1211.
- [13] A. Chieragato, M.D. Soriano, E. García-González, G. Puglia, F. Basile, P. Concepción, C. Bandinelli, J.M. López Nieto, F. Cavani, *ChemSusChem*, **2014**, 8, 398-406.
- [14] T. Murayama, K. Nakajima, J. Hirata, K. Omata, E. J. M. Hensen, W. Ueda, *Catal. Sci. Technol.*, **2017**, 7, 243-250.
- [15] C. Y. Park, J. M. Seo, H. Jo, J. Park, K. M. Ok, T. J. Park, *Sci. Rep.*, **2017**, 7, 40928.
- [16] A. Fernández-Arroyo, D. Delgado, M. E. Domine, J. M. López Nieto, *Catal. Sci. Technol.*, **2017**, 7, 5495-5499.
- [17] M. E. Domine, J. M. López Nieto, D. Delgado, A. Fernández-Arroyo, *International Patent WO2017/162900A1*, **2017**.
- [18] A. J. Ragauskas, C. K. Williams, B. H. Davison, G. Britovsek, J. Cairney, C. A. Eckert, W. J. Frederick, J. P. Hallett, D. J. Leak, C. L. Liotta, J. R. Mielenz, R. Murphy, R. Templer, T. Tschaplinski, *Science*, **2006**, 311, 484-489.
- [19] I. Graça, J. M. Lopes, H. S. Cerqueira, M. F. Ribeiro, *Ind. Eng. Chem. Res.*, **2013**, 52, 275-287.
- [20] D. C. Elliott, *Energy Fuels*, **2007**, 21, 1792-1815.
- [21] D. Radlein, A. Quignard, *US Patent 2014/0288338*, **2014**.
- [22] F. Kleitz, S. Hei Choi, R. Ryoo, *Chem. Commun.*, **2003**, 2136-2137.
- [23] M. D. Soriano, P. Concepción, J. M. López Nieto, F. Cavani, S. Guidetti, C. Trevisanut, *Green Chem.*, **2011**, 13, 2954-2962.
- [24] C. A. Emeis, *J. Catal.*, **1993**, 141, 347-354.
- [25] P. G. Dickens, M. S. Whittingham, *Q. Rev. Chem. Soc.*, **1968**, 22, 30-44.
- [26] M. Sadakane, K. Endo, K. Kodato, S. Ishikawa, T. Murayama, W. Ueda, *Eur. J. Inorg. Chem.*, **2013**, 2013, 1731-1736.
- [27] D. Saha, K. M. Ø. Jensen, C. Tyrsted, E. D. Bøjesen, A. H. Mamakhel, A.-C. Dippel, M. Christensen, B. B. Iversen, *Angew. Chem. Int. Ed.*, **2014**, 53, 3667-3670.
- [28] M. Juelsholt, T. Lindahl Christiansen, K. M. Ø. Jensen, *J. Phys. Chem. C*, **2019**, 123, 5110-5119.

- [29] I. M. Szilágyi, J. Madarász, G. Pokol, P. Király, G. Tárkányi, S. Saukko, J. Mizsei, A. L. Tóth, A. Szabó, K. Varga-Josepovits, *Chem. Mater.*, **2008**, 20, 4116-4125.
- [30] J. M. Jehng, I. E. Wachs, *Chem. Mater.*, **1991**, 3, 100-107.
- [31] M. Maczka, J. Hanuza, S. Kojima, A. Majchrowski, J. H. van der Maas, *J. Raman Spectrosc.*, **2001**, 32, 287-291.
- [32] A. A. McConnell, J. S. Aderson, C. N. R. Rao, *Spectrochim. Acta A*, **1976**, 32, 1067-1076.
- [33] M. D. Soriano, E. García-González, P. Concepción, C. B. Rodella, J. M. López Nieto, *Cryst. Growth Des.*, **2017**, 17, 6320-6331.
- [34] K. Omata, K. Matsumoto, T. Murayama, W. Ueda, *Catal. Today*, **2016**, 259, 205-212.
- [35] Y. Goto, K. Shimizu, T. Murayama, W. Ueda, *Appl. Catal. A: Gen.*, **2016**, 509, 118-122.
- [36] J. Datka, A. M. Turek, J. M. Jehng, I. E. Wachs, *J. Catal.*, **1992**, 135, 186-199.
- [37] A. Gangadharan, M. Shen, T. Sooknoi, D. E. Resasco, R. G. Mallinson, *Appl. Catal. A: Gen.*, **2010**, 385, 80-91.
- [38] K. Suwannakarn, E. Lotero, J. G. Goodwin, *Ind. Eng. Chem. Res.*, **2007**, 46, 7050-7056.

Table 1. Physicochemical features of bulk and supported W-Nb-O bronzes

Sample	Nb/(Nb+W) at. ratio ^a	KIT-6 loading wt %	Crystalline phase	Surface area (m² g⁻¹)	Mesopore volume (cm³ g⁻¹)
KIT-6	---	100	KIT-6	971	1.39
<i>h</i>-WO₃	0	0	HTB	28	0.04
A-0	0.10	0	HTB	74	0.10
A-13	0.10	13	HTB	124	0.17
A-26	0.10	26	HTB	221	0.30
B-0	0.20	0	HTB	82	0.07
B-22	0.20	22	HTB	179	0.20
B-36	0.20	36	HTB	259	0.28
B-53	0.20	53	HTB	391	0.47
C-0	0.60	0	PC	112	0.06
C-22	0.60	22	PC	212	0.11

a) Nb/(W+Nb) atomic ratio in gel; the corresponding composition of calcined samples are included in Table S1.

Table 2. Acid characteristics of selected W-Nb-O catalysts

Sample	Nb/(W+Nb) at. ratio	KIT-6 loading (wt.%)	Concentration of acid sites ($\mu\text{mol}_{\text{py}} \text{g}^{-1}$)			LAS/(BAS+LAS) ratio
			LAS	BAS	Total	
<i>h</i> -WO ₃	0	0	49.5	33.8	83.3	0.57
A-26	0.10	26	76.6	65.2	141.8	0.54
B-22	0.20	22	125.3	76.8	202.1	0.62
C-0	0.60	0	80.7	32.9	113.6	0.71
C-22	0.60	22	120.0	42.2	162.2	0.74

Table 3. Catalytic results for the transformation of the aqueous model mixture on W-Nb-O catalysts

Catalyst		<i>h</i> -WO ₃	Series A			Series B			Series C		
			A-0	A-13	A-26	B-0	B-22	B-36	B-53	C-0	C-22
Conversion (%)	Acetic acid	0.0	4.0	9.1	0.0	7.6	0.0	7.0	0.0	10.7	5.1
	Propanal	86.6	86.0	91.9	88.5	89.0	88.5	81.3	82.5	90.2	87.0
	Ethanol	49.8	50.9	50.2	50.1	47.6	47.8	46.8	48.2	46.9	43.9
	Acetol	100.0	100.0	100.0	100.0	100.0	100.0	100.0	100.0	100.0	100.0
Organic Products	Ethyl acetate	22.3	20.7	22.0	20.3	22.0	22.0	22.6	23.0	23.3	23.3
	2M2P	29.6	29.6	30.7	30.3	32.0	32.0	31.3	28.0	36.3	34.6
Yield (%)	C ₅ -C ₈	12.0	14.7	17.0	15.3	15.7	15.7	16.0	14.7	14.0	15.0
	C ₉ -C ₁₀	11.3	10.7	11.0	9.7	12.3	12.0	11.4	11.6	16.0	15.4
Total Org. Prod. Yield (%)		52.9	55.0	58.7	55.3	60.0	59.7	58.7	54.3	66.3	65.0
C Balance (%)		90.9	91.0	90.6	94.5	93.2	95.9	95.1	96.6	96.6	99.2

Reaction conditions: 3000 mg of initial mixture, 150 mg of catalyst, 200°C and P_{N2} = 13 bar during 7 h. ^a Total Organic Products Yield is the sum of the yields of 2M2P, C₅-C₈ and C₉-C₁₀ products.

Caption to Figures

Figure 1. XRD patterns of bulk and supported W-Nb-O catalysts from A, B and C series (A, B and C respectively). The pattern of a hydrothermally synthesized *h*-WO₃ is also included for comparison. a) A-0; b) A-13; c) A-26; d) B-0; e) B-22; f) B-36; g) B-53; h) C-0; i) C-22.

Figure 2. Raman spectra of selected bulk (A) and supported (B) W-Nb-O oxides. Raman spectrum of an *h*-WO₃ prepared by hydrothermal synthesis is also shown. a) A-0; b) B-0; c) C-0; d) A-13; e) B-22; f) C-22.

Figure 3. SEM images of bulk (*a* and *b*) and supported (*d*) W-Nb-O catalysts. An image of an as-prepared KIT-6 silica is also shown (*c*). a) A-0; b) C-0; c) KIT-6; d) A-26

Figure 4. HRTEM images of as-prepared KIT-6 (*a*), and supported crystalline (*b*) and pseudocrystalline (*c*) W-Nb-O catalysts. a) KIT-6; b) B-22; c) C-22

Figure 5. FTIR spectra of adsorbed pyridine after desorption at 150 °C (black spectra, a-d) and at 250 °C (red spectra, a'-d') of selected bulk and supported W-Nb-O catalysts. A spectrum (after desorption at 150 °C) of a *h*-WO₃ prepared by hydrothermal synthesis is included. a-a') A-26; b-b') B-22; c-c') C-0; d-d') C-22.

Figure 6. Conversion of acetol, propanal, ethanol and acetic acid for bulk and supported W-Nb-O catalysts. Conversion attained on a *h*-WO₃ sample are also displayed. Reaction conditions: 13 bar N₂ and 200 °C under continuous stirring; time on stream of 7 h.

Figure 7. Yield to 2-methyl-2-pentenal (A), C₅-C₈ (B) and C₉-C₁₀ products (C) attained on bulk and supported W-Nb-O catalysts. Results obtained with a *h*-WO₃ are also shown. Reaction conditions: 13 bar N₂ and 200 °C under continuous stirring; time on stream of 7 h.

Figure 8. Total organic yield (2-methyl-2-pentenal + C₅-C₈ + C₉-C₁₀) attained on bulk and supported W-Nb-O catalysts. The total organic yield obtained with a *h*-WO₃ catalyst is also included. Reaction conditions: 13 bar N₂ and 200 °C under continuous stirring; time on stream of 7 h.

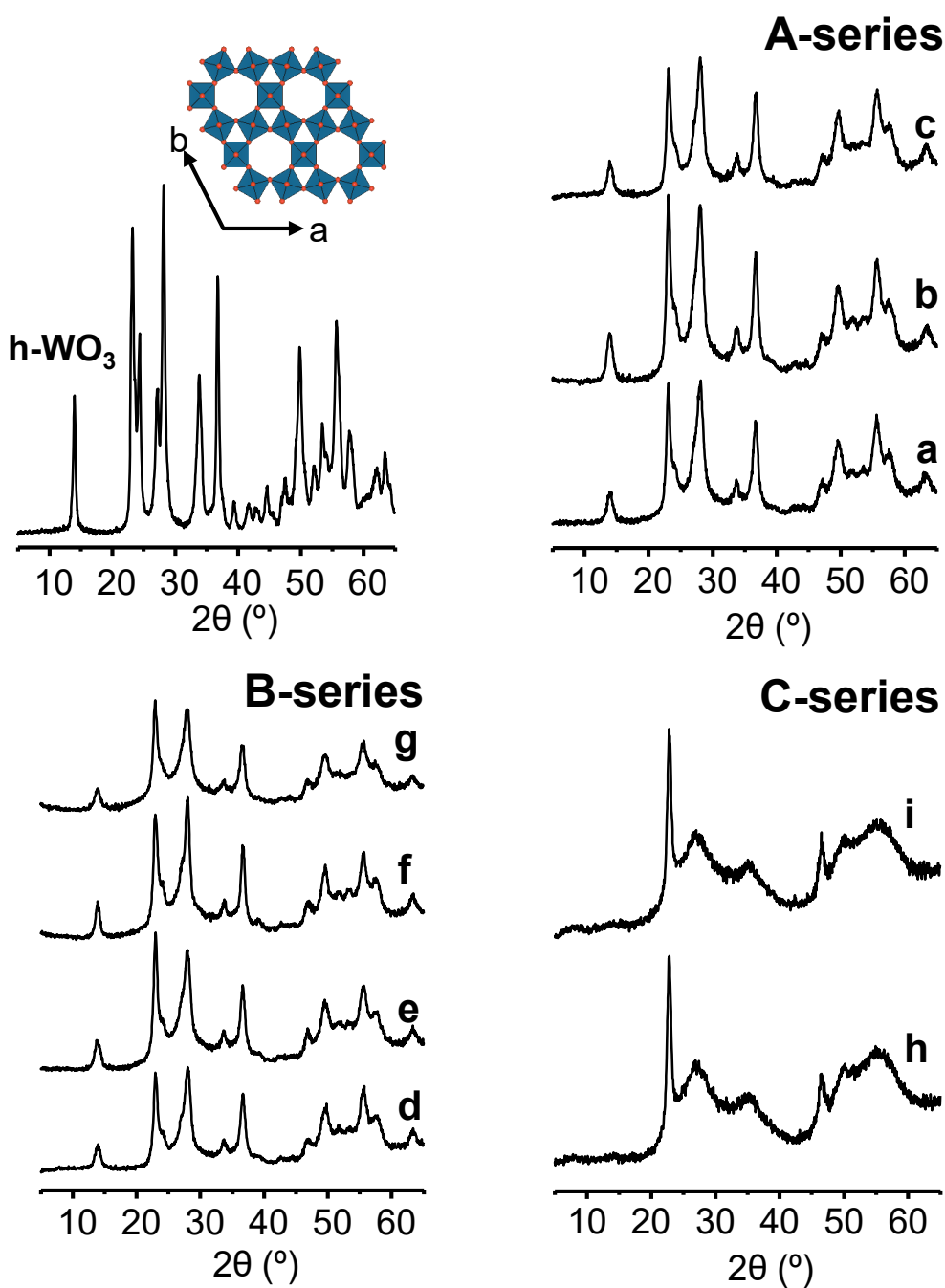


Figure 1. XRD patterns of bulk and supported W-Nb-O catalysts from A, B and C series (A, B and C respectively). The pattern of a hydrothermally synthesized $h\text{-WO}_3$ is also included for comparison. a) A-0; b) A-13; c) A-26; d) B-0; e) B-22; f) B-36; g) B-53; h) C-0; i) C-22. **Characteristics of catalysts in Table 1.**

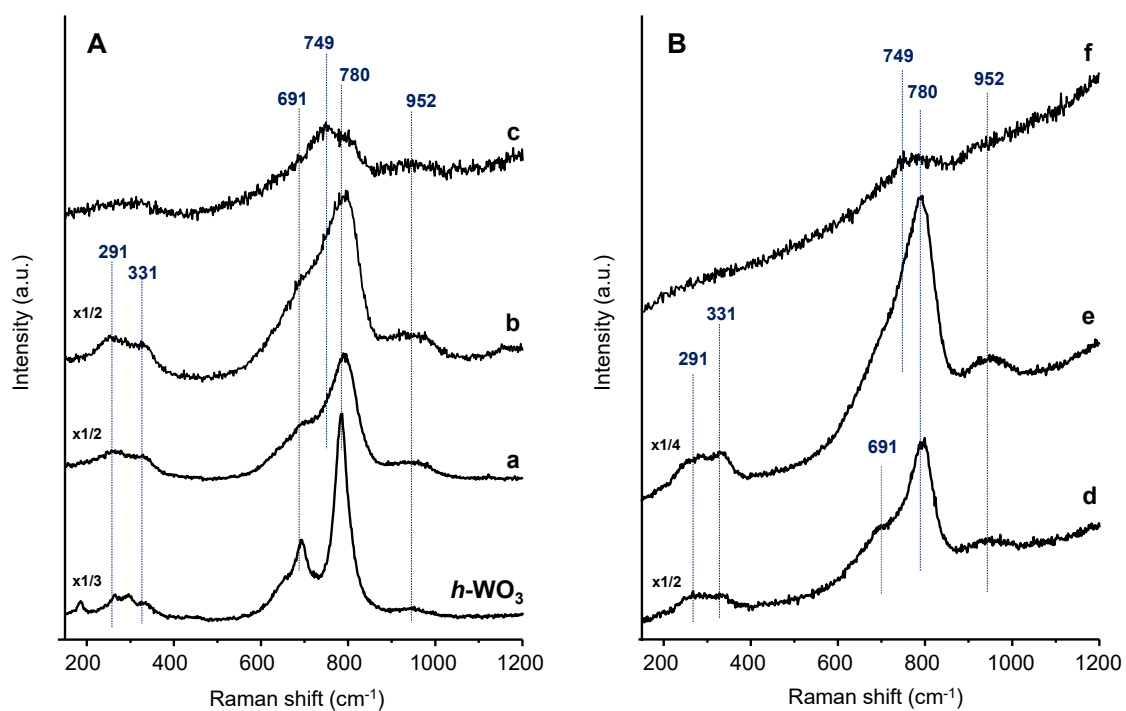


Figure 2. Raman spectra of selected bulk (A) and supported (B) W-Nb-O oxides. Raman spectrum of an $h\text{-WO}_3$ prepared by hydrothermal synthesis is also shown. a) A-0; b) B-0; c) C-0; d) A-13; e) B-22; f) C-22. Characteristics of catalysts in Table 1.

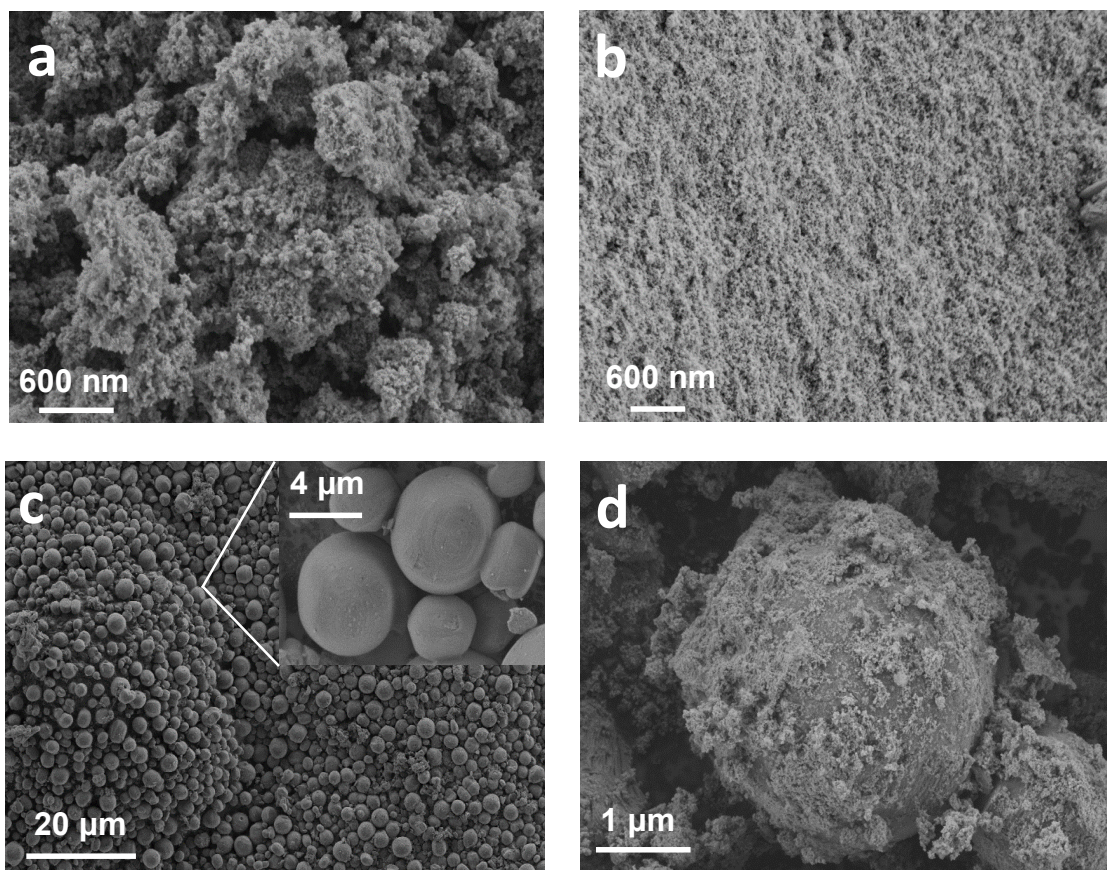


Figure 3. SEM images of bulk (*a* and *b*) and supported (*d*) W-Nb-O catalysts. An image of an as-prepared KIT-6 silica is also shown (*c*). *a*) A-0; *b*) C-0; *c*) KIT-6; *d*) A-26.

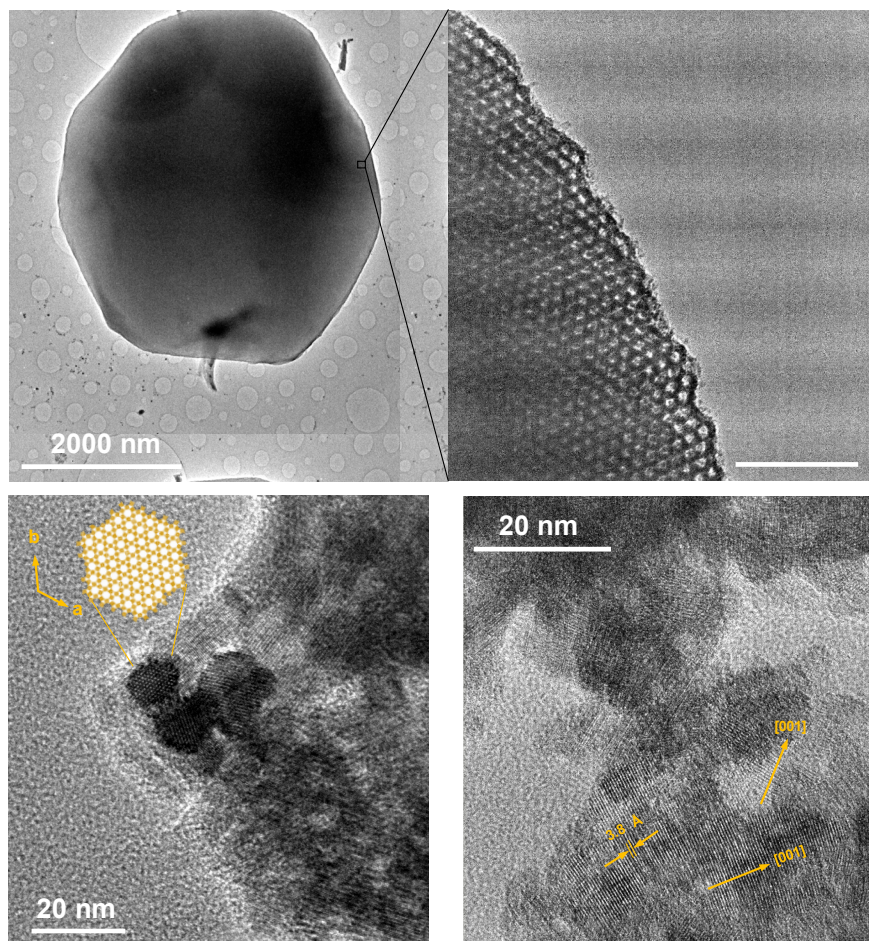


Figure 4. HRTEM images of as-prepared KIT-6 (*a*), and supported crystalline (*b*) and pseudocrystalline (*c*) W-Nb-O catalysts. a) KIT-6; b) B-22; c) C-22

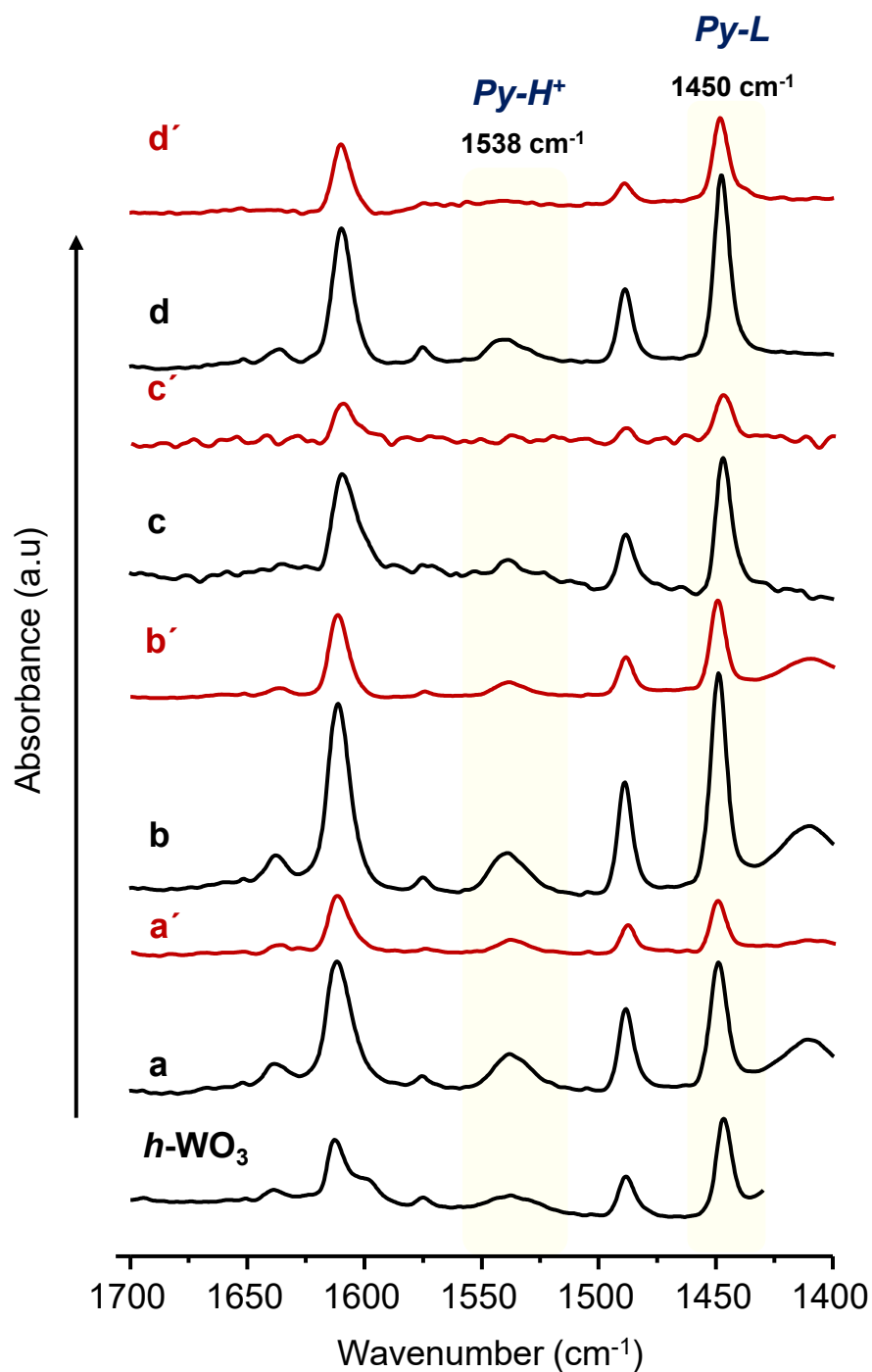


Figure 5. FTIR spectra of adsorbed pyridine after desorption at 150 °C (black spectra, a-d) and 250 °C (red spectra, a'-d') of selected bulk and supported W-Nb-O catalysts. A spectrum (after desorption at 150 °C) of a *h*-WO₃ prepared by hydrothermal synthesis is included. a-a') A-26; b-b') B-22; c-c') C-0; d-d') C-22.

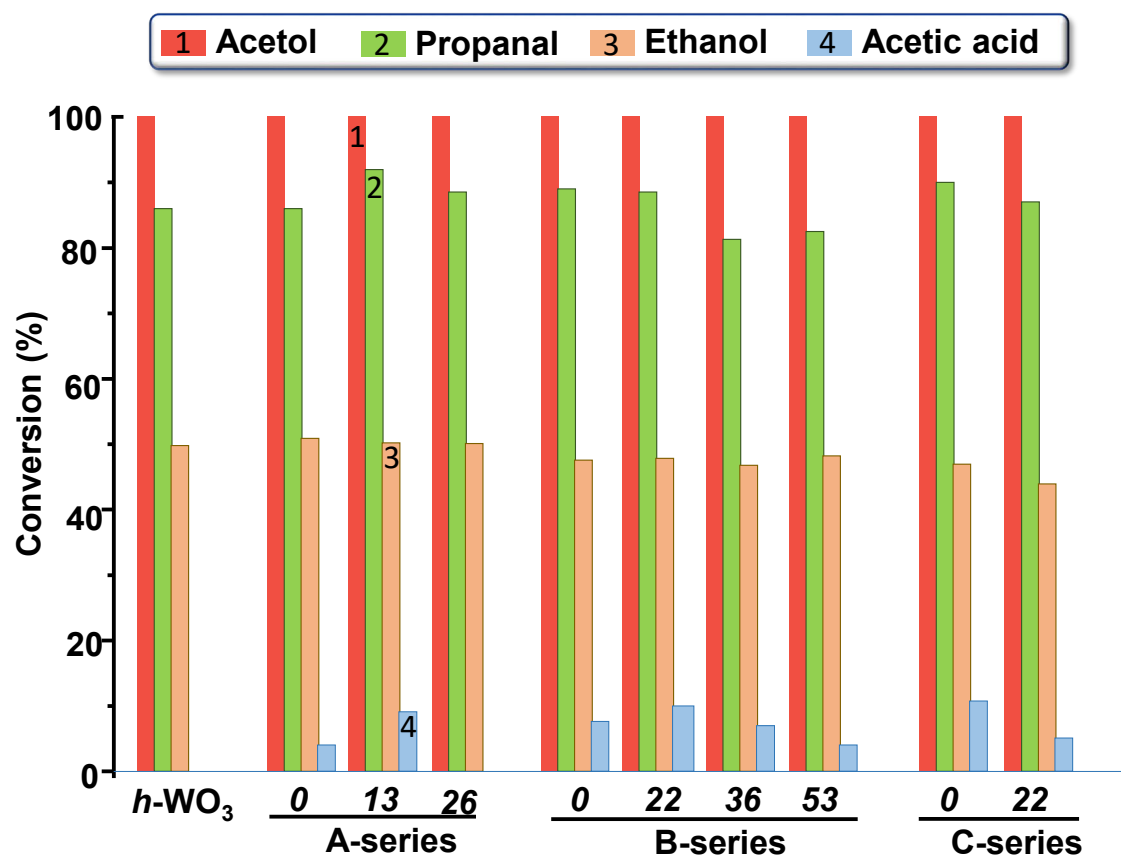


Figure 6. Conversion of acetol, propanal, ethanol and acetic acid for bulk and supported W-Nb-O catalysts. Conversion attained on a *h*-WO₃ sample are also displayed. Reaction conditions: 13 bar N₂ and 200 °C under continuous stirring; time on stream of 7 h.

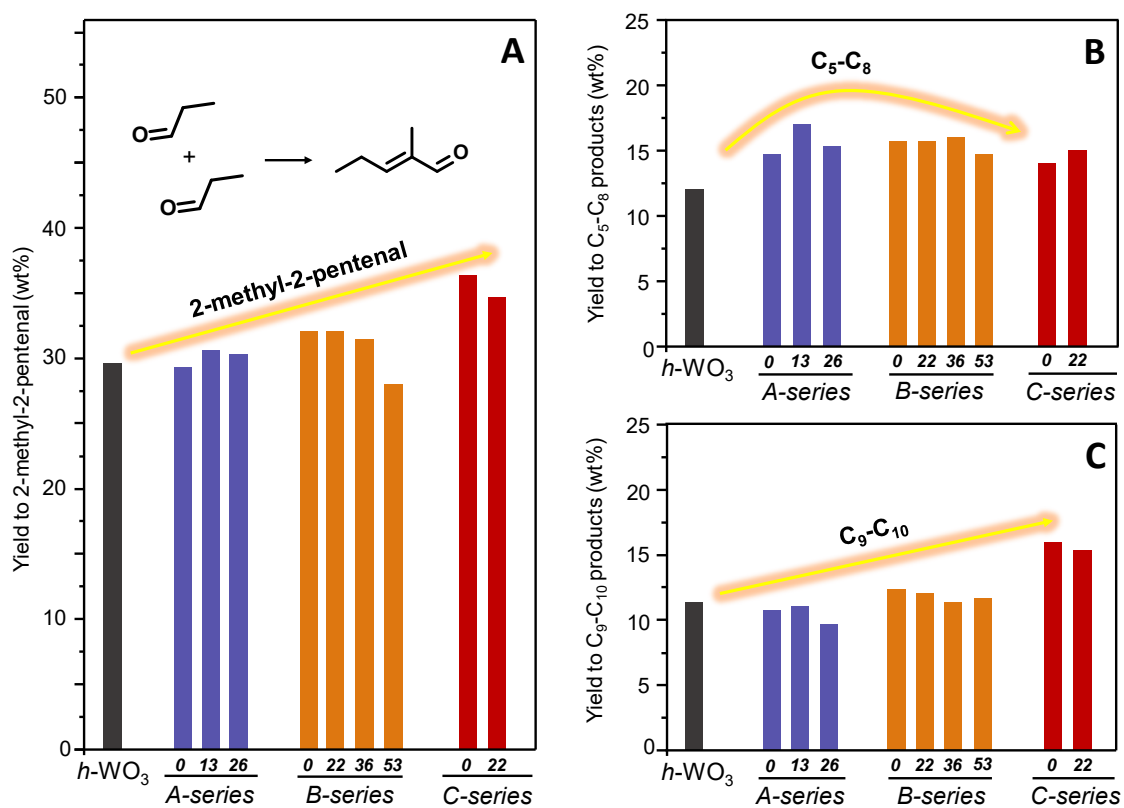


Figure 7. Yield to 2-methyl-2-pentenal (A), $\text{C}_5\text{-C}_8$ (B) and $\text{C}_9\text{-C}_{10}$ products (C) attained on bulk and supported W-Nb-O catalysts. Results obtained with a $h\text{-WO}_3$ are also shown. Reaction conditions: 13 bar N_2 and 200 °C under continuous stirring; time on stream of 7 h.

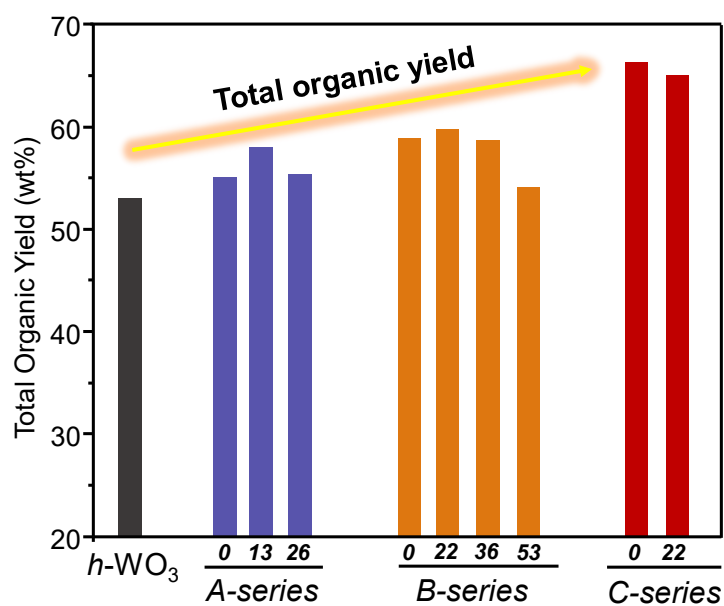


Figure 8. Total organic yield (2-methyl-2-pentenal + C₅-C₈ + C₉-C₁₀) attained on bulk and supported W-Nb-O catalysts. The total organic yield obtained with a $h\text{-WO}_3$ catalyst is also included. Reaction conditions: 13 bar N₂ and 200 °C under continuous stirring; time on stream of 7 h.

SUPPORTING INFORMATION

Reflux-synthesized bulk and supported W-Nb-O mixed oxide bronzes for the valorization of short-chain oxygenates aqueous mixtures

D. Delgado, A. Fernández-Arroyo, N. La Salvia, M.E. Domine, J.M. López Nieto

Instituto de Tecnología Química, Universitat Politècnica de València-Consejo Superior
de Investigaciones Científicas, Avenida de los Naranjos s/n, 46022, Valencia, Spain.

E-mail: jmlopez@itq.upv.es

Experimental part (supporting information): Reaction mixture analysis

Catalytic results along this work are discussed in terms of reactant conversion and main reaction products yield. In this context, the following formulas have been used:

$$\text{Conversion (mol\%)} = \frac{(\text{Reactant}_x \text{ initial moles} - \text{Reactant}_x \text{ final moles})}{\text{Reactant}_x \text{ initial moles}} * 100$$

Reaction S1. Reactant conversion (mol%) calculation.

$$\text{Product}_y \text{ yield (wt\%)} = \frac{\text{Mass of Product}_y \text{ in the reactor}}{\text{Total mass in the reactor}} * 100$$

Reaction S2. Main products yields (wt%) calculation.

$$\text{Total organic products yield (wt\%)} = \text{Yield}_{2M2P} + \text{Yield}_{C5-C8} + \text{Yield}_{C9-C10}$$

Reaction S3. Total organic product yield (wt%) calculation.

In addition, and based on the initial aqueous model mixture composition, a theoretical maximum attainable total organic products yield is determined, considering: a) 100% conversion for all reactants; b) acetic acid is equally converted to ethyl acetate and acetone; and c) final products are only C9 compounds (no intermediates or products heavier than C9 are present in the final mixture). In this ideal scenario, the composition of the final mixture after reaction is calculated as follows: 51.3wt% of water, 19.1wt% of ethyl acetate, and 29.6wt% of C9 products. Therefore, results of catalytic experiments are expressed in terms of yields to the main reaction products separately; and total organic products yield, which are calculated and referred to 30.0wt% as the maximum attainable value by considering the initial composition of the aqueous mixture used.

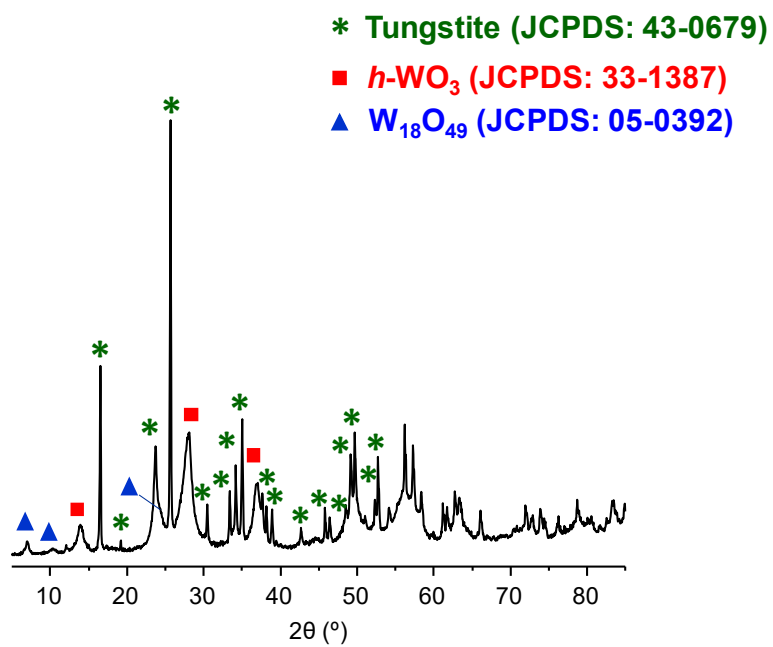


Figure S1. XRD pattern of as-synthesized undoped tungsten oxide by reflux method.

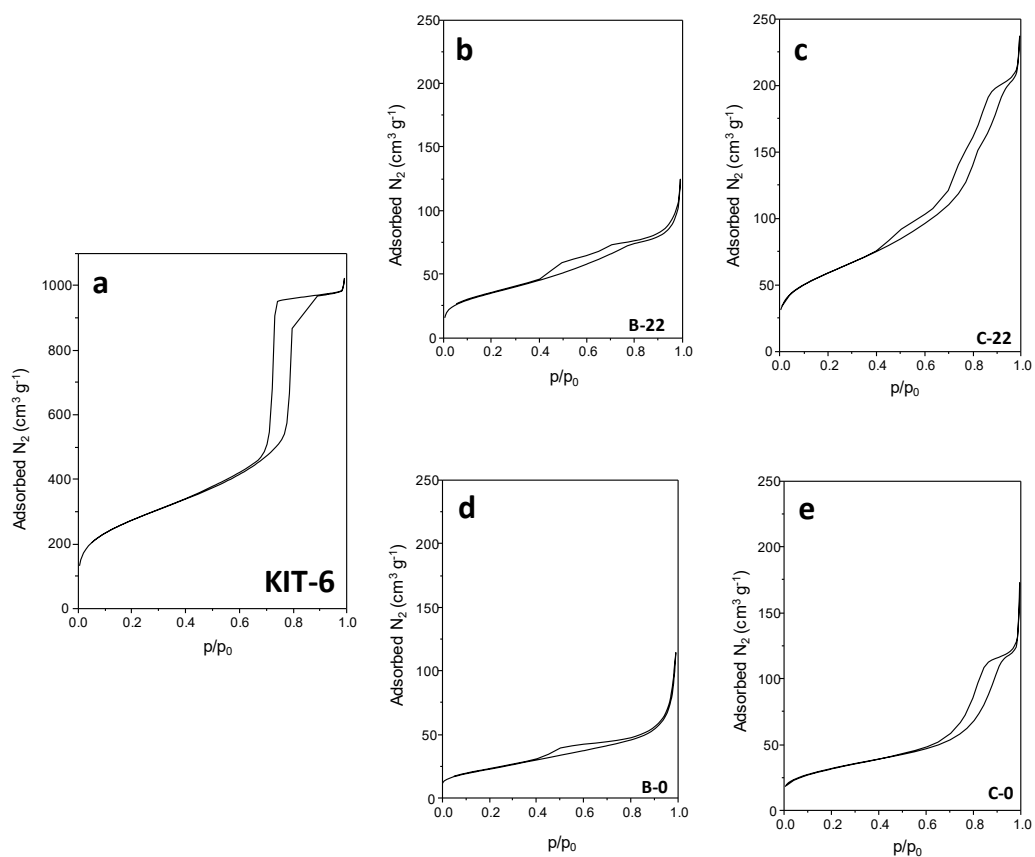


Figure S2. N₂-adsorption-desorption isotherms of selected bulk and supported W-Nb-O catalysts. KIT-6 isotherm is also shown. a) KIT-6; b) B-22; c) C-22; d) B-0; e) C-0.

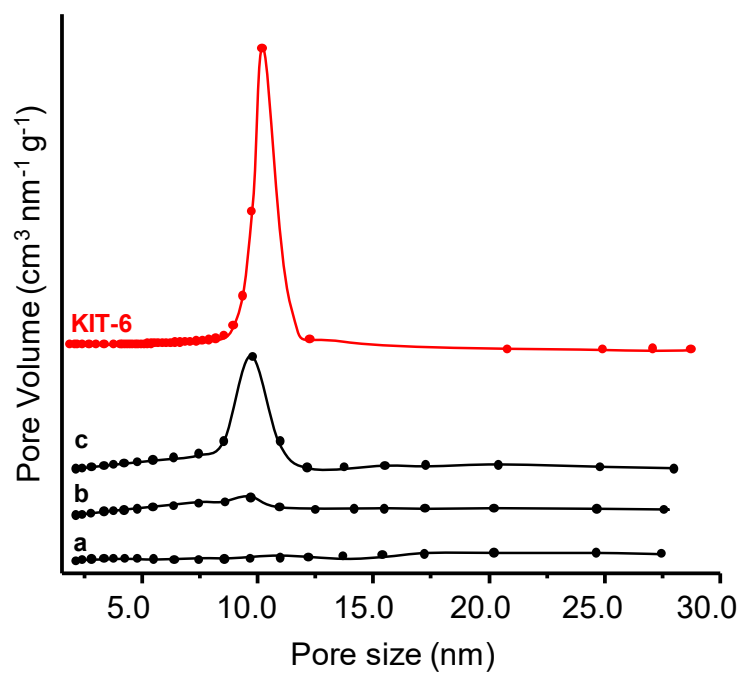
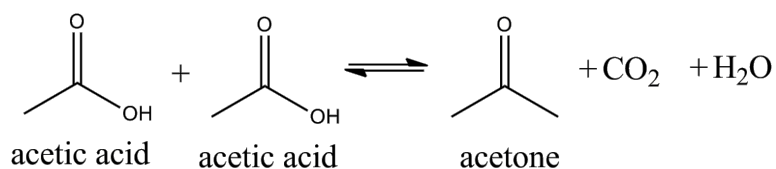


Figure S3. Pore size distribution calculated by BJH method for bulk and supported W-Nb-O catalysts from A-series (W/Nb at. ratio of 0.15). a) A-0; b) A-13; c) A-26.

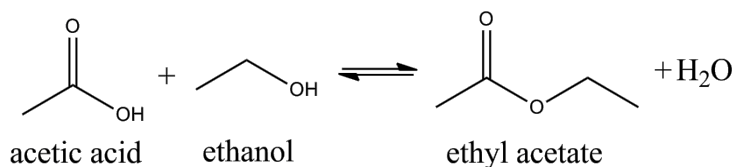
Reaction Network:

A detailed reaction network can be proposed by including the main reaction pathways and products observed along the experiments, which are detailed below:

- 2 molecules of acetic acid can react via ketonization to produce one molecule of acetone and CO₂ and H₂O as only subproducts. Acetic acid can also react with ethanol via esterification to produce ethyl acetate.

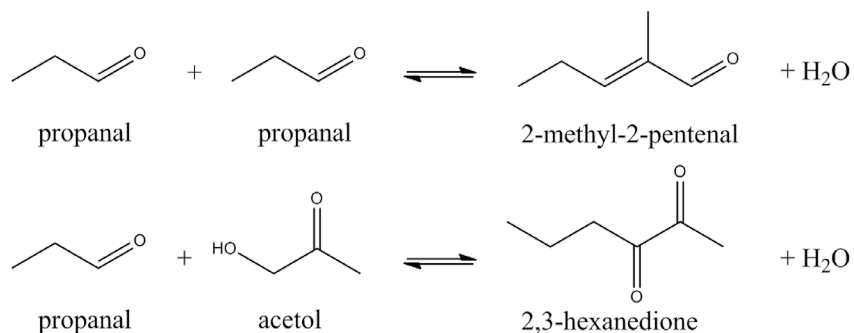


Reaction 1. Acetic acid ketonization reaction



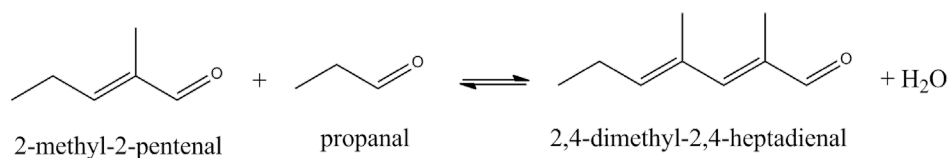
Reaction 2. Acetic acid and ethanol esterification reaction

- Acetone, together with propanal and acetol can react via self- or cross- aldol condensation to produce intermediate products as 2-methyl-2-pentenal, mesityl oxide, 3-hexen-2-one, or 2,3-hexanedione. Water is also produced from condensation reactions.



Reaction 3. Propanal self- and cross-aldol condensation reaction.

- These intermediate products can keep reacting in a 2nd condensation step to produce larger C₉-C₁₀ products. Equimolar amounts of water are likewise generated in these cases.



Reaction 3.4. 2nd aldol condensation step reaction.

Moreover, and due to the mixture complexity (presence of high amounts of water and different functional groups as acids, aldehydes, alcohols and ketones) other reactions can simultaneously occur as alkylations, decarbonylations, and cyclations, among others.

Then, besides first-step condensation products as acetone, 3-pentanone and 2-methyl-2-pentenal, groups of molecules containing from 5 to 10 carbon atom are distinguished and classified in two main groups, namely C₅-C₈ and C₉-C₁₀ products, to simplify its quantification.

Taking into account all the above-mentioned reaction pathways, the next reaction network for the overall process is proposed (Figure S4).

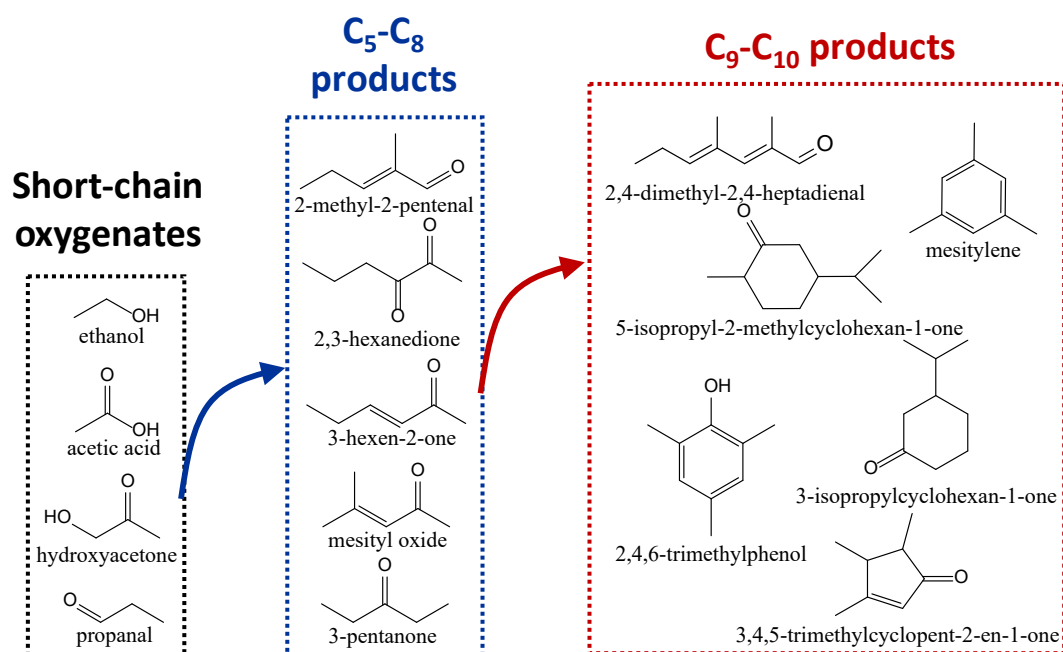


Figure S4. Scheme of the aqueous model mixture transformation by C-C bond formation reactions.

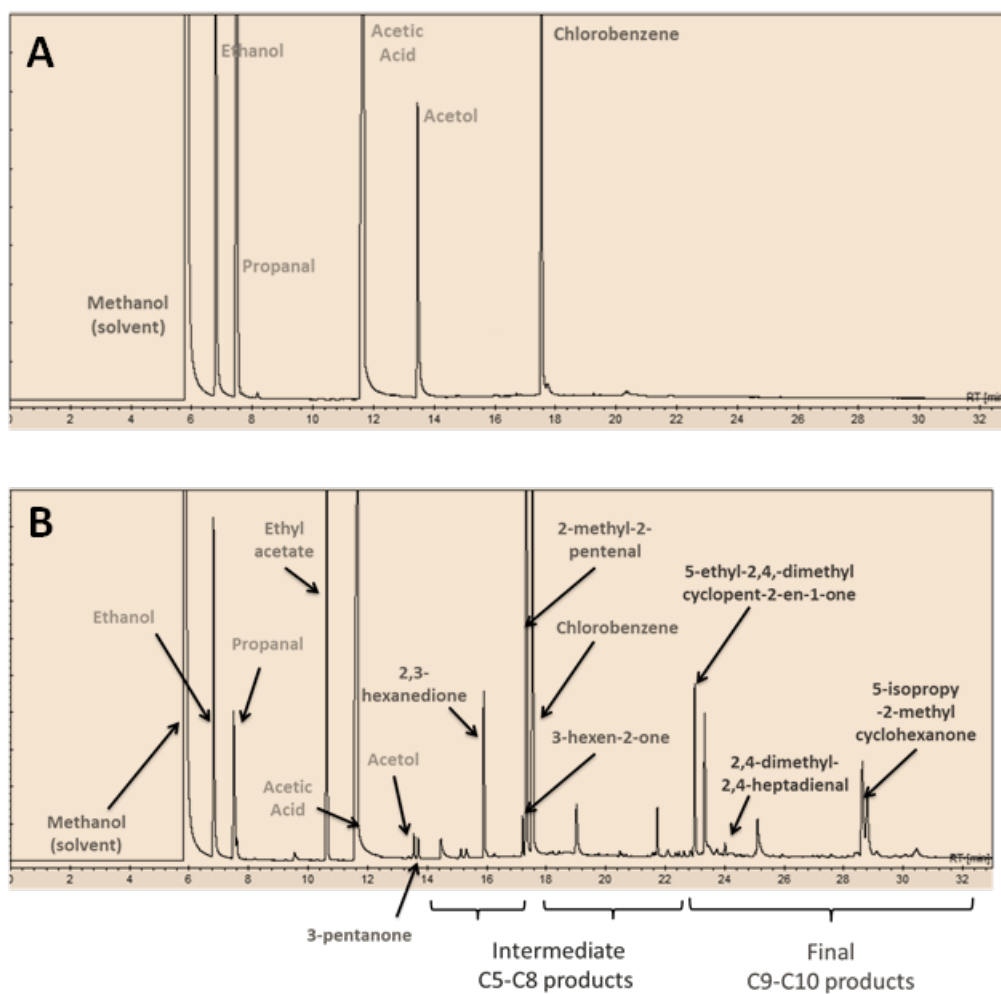


Figure S5. A) Chromatogram of the reaction mixture (0 h). (B) Chromatogram of the reaction mixture after 7h of reaction at 200 °C.

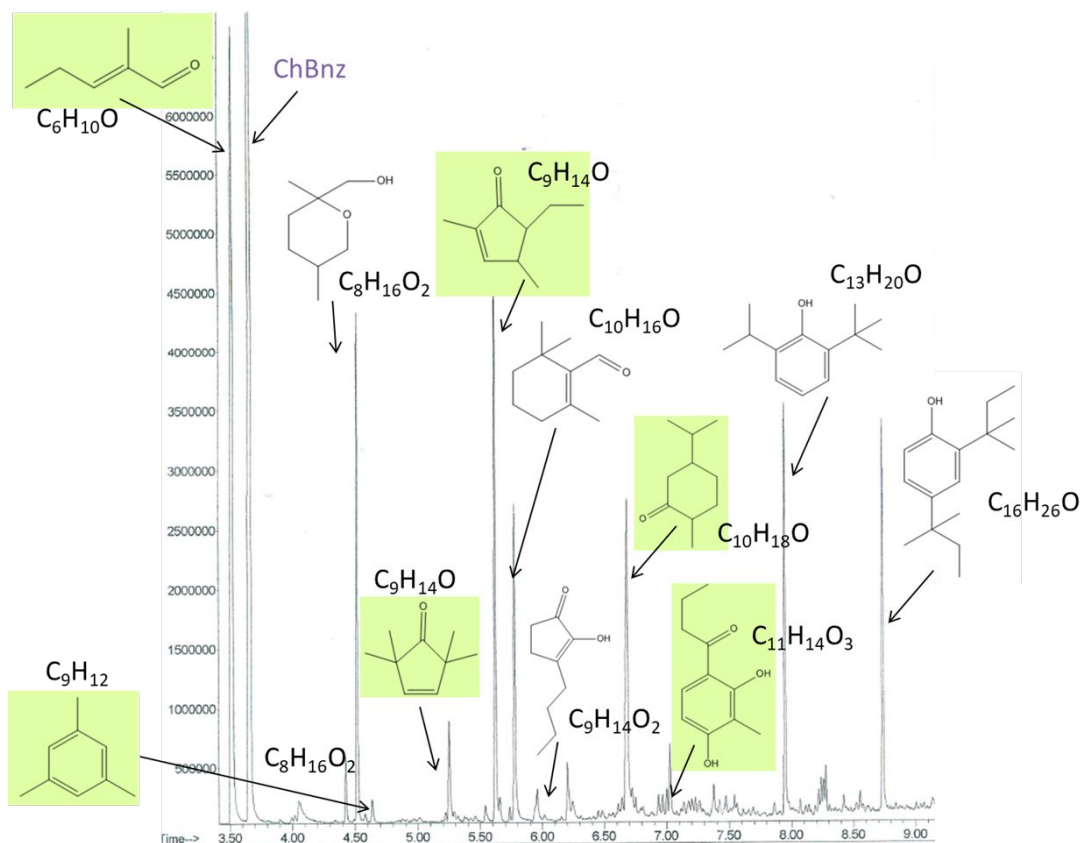


Figure S6. Main identified compounds (C_6 - $C_{10}+$) present in organic phase by GC-MS analysis.

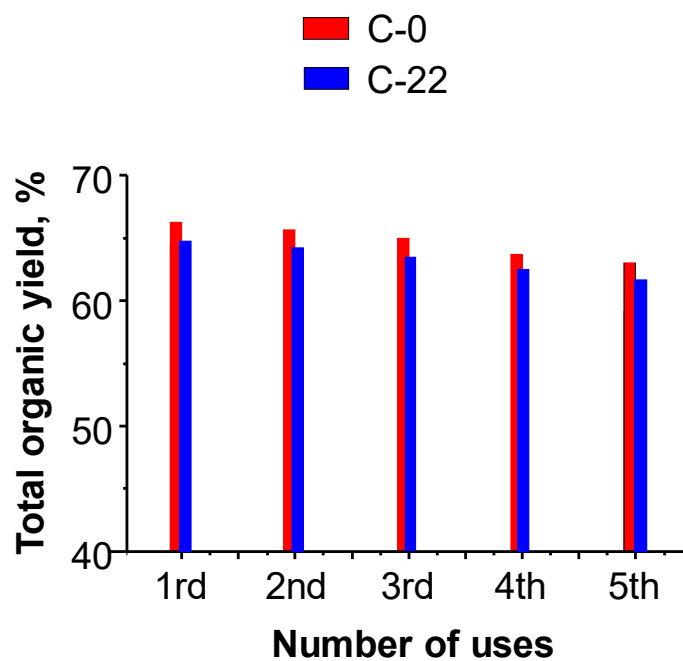


Figure S7. Total organic yield attained on unsupported (C-0) and supported (C-22) W-Nb-O catalysts from C-series (W/Nb at. ratio of 1/1.45) after 5 consecutive uses.

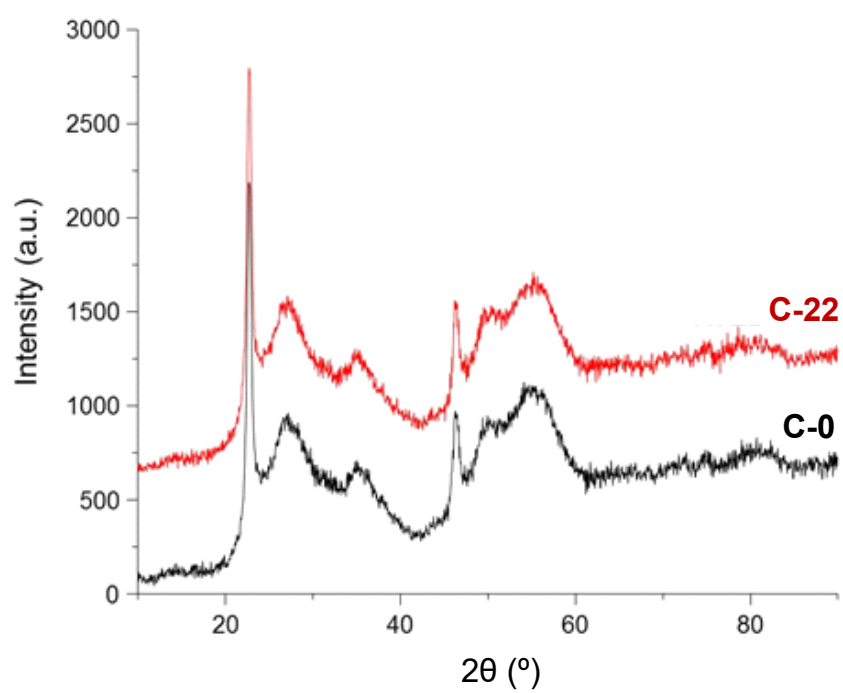


Figure S8. XRD patterns of C-0 and C-22 catalysts after the third use